



HAL
open science

Laser Direct Writing of Silver Clusters-Based Subwavelength Periodic Structures Embedded in Mid-Infrared Gallo-Germanate Glass

Théo Guérineau, Alexandre Fargues, Jerome Lapointe, Réal Vallée, Younès Messaddeq, Lionel Canioni, Yannick Petit, Thierry Cardinal

► **To cite this version:**

Théo Guérineau, Alexandre Fargues, Jerome Lapointe, Réal Vallée, Younès Messaddeq, et al.. Laser Direct Writing of Silver Clusters-Based Subwavelength Periodic Structures Embedded in Mid-Infrared Gallo-Germanate Glass. *Advanced Photonics Research*, 2022, 3 (10), 2200032 (13 p.). 10.1002/adpr.202200032 . hal-03682520

HAL Id: hal-03682520

<https://hal.science/hal-03682520v1>

Submitted on 31 May 2022

HAL is a multi-disciplinary open access archive for the deposit and dissemination of scientific research documents, whether they are published or not. The documents may come from teaching and research institutions in France or abroad, or from public or private research centers.

L'archive ouverte pluridisciplinaire **HAL**, est destinée au dépôt et à la diffusion de documents scientifiques de niveau recherche, publiés ou non, émanant des établissements d'enseignement et de recherche français ou étrangers, des laboratoires publics ou privés.

Laser Direct Writing of Silver Clusters-Based Subwavelength Periodic Structures Embedded in Mid-Infrared Gallo-Germanate Glass

Théo Guérineau, Alexandre Fargues, Jerome Lapointe, Réal Vallée, Younès Messaddeq, Lionel Canioni, Yannick Petit, and Thierry Cardinal*

The direct laser writing (DLW) using femtosecond lasers allows for the inscription of 3D microstructures embedded inside optical materials. Based solely on the silver ions photochemistry, the DLW in silver-containing glasses enables to locally induce inside glasses a unique combination of optical properties. The physical modifications of the material encompass not only a refractive index change, but also new physical properties like fluorescence, second- and third-harmonic generations, and surface plasmon resonance. Numerous efforts are deployed to develop the DLW-assisted silver photochemistry in phosphate glasses. However, this glass family is suffering from its near-infrared optical cutoff as opposed to the silver-doped gallo-germanate glasses. With an extended mid-infrared (mid-IR) transmission, these glasses are synthesized via the melt-quenching technique. Depending on the glass composition, either a glass matrix-based single track (Type I) or a silver cluster-based double track (Type A) of refractive index change is produced. By enabling an order of magnitude smaller structures than with Type I, Type A modification is further expanded to embed, for the first time, periodic structures below the inter-track spacing. Demonstrated with a pitch down to 400 nm, these Type A–based periodic structures bring new insights through the fabrication of 3D diffractive gratings in mid-IR glasses.

media. In contrast to the several lithography techniques consisting of layer-by-layer depositions,^[4] the femtosecond direct laser writing (DLW) allows to inscribe freeform buried optical structures in transparent dielectric materials.^[5] In that respect, the DLW fabrication of 3D photonic components inside optical glasses opens up a wide avenue for applications in many fields: optofluidic,^[6] sensing,^[7,8] optical communication,^[9] astrophotonics,^[10] quantum photonics,^[11] and optical data storage.^[12,13] Moreover, 3D waveguides with submillimeter radii of curvature have been recently achieved, which gives a new momentum to the densification of compact photonics components.^[14]


Taking advantage of the nonlinear absorption during the laser irradiation, the laser pulse energy confined in the interaction region can lead to several kinds of glass modifications: redox reaction,^[15,16] ionic migration,^[17,18] glass densification,^[19] surface nanograting and nanopore formation,^[20,21] defect centers generation,^[22]

and glass crystallization.^[23–25] By controlling both the laser parameters and the glass composition, the glass modification can be tailored and is usually classified in three laser inscription regimes (Type I, Type II, and Type III) depending on the precise nature of the modification. Type I corresponds to a smooth, isotropic, and continuous change of the material density and thus of its refractive index,^[26] Type II is associated with a formation of

1. Introduction

As demonstrated by Davis et al. in 1996, the light–matter interaction via an ultrafast laser pulse allows for the formation of permanent and confined modification in glasses.^[1] Down to sub-micrometric dimensions,^[2,3] the laser-induced material alteration allows 3D structuring inside dielectric transparent

T. Guérineau, A. Fargues, Y. Petit, T. Cardinal
Institut de Chimie de la Matière Condensée de Bordeaux (ICMCB – UMR5026)
Centre National de la Recherche Scientifique (CNRS)
Université de Bordeaux
87 avenue du Dr Albert Schweitzer, 33600 Pessac, France
E-mail: theo.guerineau@gmail.com

 The ORCID identification number(s) for the author(s) of this article can be found under <https://doi.org/10.1002/adpr.202200032>.

© 2022 The Authors. Advanced Photonics Research published by Wiley-VCH GmbH. This is an open access article under the terms of the Creative Commons Attribution License, which permits use, distribution and reproduction in any medium, provided the original work is properly cited.

DOI: 10.1002/adpr.202200032

T. Guérineau, J. Lapointe, R. Vallée, Y. Messaddeq
Department of Physics
Université Laval
2375 Rue de la Terrasse, Québec QC G1V 0A6, Canada

L. Canioni, Y. Petit
Centre lasers intenses et applications (CELIA – UMR5107)
Centre National de la Recherche Scientifique (CNRS)
Université de Bordeaux
Commissariat à l'énergie atomique et aux énergies alternatives (CEA)
43 rue Pierre Noailles, Domaine du Haut Carrée, 33400 Talence, France

birefringent periodic nanostructures,^[20] while Type III relates to void-like structures arising from Coulombic explosions.^[27] Over time, researchers have extensively explored the femtosecond direct laser writing in a wide range of glass families, that is, silicate, borate, fluoride, chalcogenide, phosphate, germanate, etc.,^[1,28–31] revealing the universality of this laser-induced glass processing.

In silver-containing phosphate glasses, the silver ions act as photosensitive agents and trigger an exotic material modification based solely on the silver ion photochemistry.^[32] As enlightened by Bellec et al.,^[33] the laser irradiation generates free electrons inside the glass that recombine with Ag^+ silver ions to form Ag^0 silver atoms. By the accumulation of the femtosecond laser pulses, the migration of silver atoms and ions is initiated from the inner modification region to the outer one.^[32] In the meantime, the clusterization of the silver atoms and ions occurs, leading to the creation of various silver entities. However, the competition between both the photodiffusion and photodissociation phenomena allows stabilizing silver clusters only at the periphery of the laser irradiation zone. The final silver clusters can have various nuclearities and electrical charges from the smallest one, that is, Ag_2^+ , to the more complex Ag_m^{x+} with $x < m$. After stationary laser irradiation of at least 10^4 pulses, the persistent modification consists only of a silver cluster-formed cylinder elongated along the laser beam propagation axis.^[34] This micrometric elongated distribution possesses a diffraction-limit-beating wall, reaching an 80 nm thickness.^[33] When the laser irradiation is no longer stationary but rather follows a perpendicular translation to the propagation beam axis, the resulted modification is a double plane with two rounded endings.^[34] At the exact location of each plane, a refractive index change appears due to the formation of new silver–silver chemical bonds.^[35] This exotic refractive index change, specifically resulting from the laser-induced photochemistry of silver ions without significantly affecting the glass matrix, is categorized as the Argentum Type (Type A). The formation of laser-generated silver clusters also gives rise to other remarkable optical properties such as photoluminescence, second- and third-harmonic generation, and the creation of silver plasmonic nanoparticles.^[16,33,36,37] Finally, the influence of the silver-doped phosphate glass structure under different types of irradiations (DLW and X-Ray) on the glass photosensitivity has been recently published elsewhere.^[38–40] It has been reported that the increase of non-bridging oxygens (NBOs, oxygens linked only to one glass-former chemical element) via the change of glass structure leads to a significant increase of the glass photosensitivity. The photosensitivity enhancement is notably observed through the increase of several photoinduced silver entities, like electron-hole silver defects $\text{Ag}^{2+}/\text{Ag}^0$ and molecular silver clusters Ag_m^{x+} .

Several applications have already emerged from the localized change of the refractive index induced by laser in silver-containing phosphate glasses, such as single-mode waveguiding or ultrasensitive refractive index sensor.^[41] However, the main drawback of the phosphate glass family is its restricted mid-infrared (mid-IR) optical transmission window ending at 3 μm , limiting their potential of applications. On the one hand, the atmospheric transparency window between 3 and 5 μm allows for the development of military counter measurement system and the astronomical observations performed on Earth, while on the other hand, the strong absorption of water at 3 μm allows for the

elaboration of Erbium-doped optical fiber for medical surgery. Hence, the need of glass composition with a UV-to-mid-IR transparency up to 5 μm is requested. Originally developed by the U.S. Naval Laboratory, germanium–gallium–barium (BGG) oxide glasses possess tremendous properties, including mid-IR transmission up to 6 microns, strong mechanical properties, and high glass transition temperature.^[42,43] In this last decade, several research groups have already performed laser inscription in BGG glasses, proving the 3D fabrication of optical couplers or waveguides.^[29,31,44] However, none of them have explored the potential of silver-doped BGG glasses for DLW.

In this article, we report the fabrication of silver-doped BGG glass samples and their subsequent irradiation leading to either a hybrid combination of both Type A and Type I modifications, or solely to a Type A modification. We show that by precisely tailoring the glass compositions and structures, the type of laser-induced glass modification can be selected. Through the increase of barium ion concentration, the silver solubility in glass is enhanced. At low barium concentration, the hybrid Type A/I modification is favored, while at high barium ion concentration, only the Type A is promoted. We suggest a mechanism explaining the hybrid Type A/I modification based on silver-assisted Type A modification through a decrease of the laser pulse energy threshold. In a high-barium-containing BGG glass and at low laser fluence, a single track of refractive index change and fluorescence is reported, suggesting the observation of the very early stages of Type A formation. At higher laser fluence, Type A modifications are observed with the typical double track of refractive index change and fluorescence. The refractive index change reaches 2×10^{-3} and 1×10^{-4} for the double (Type A) and single (Type-A early stages) track, respectively. In the high-barium-containing BGG glasses, embedded periodic structures with a pitch down to 400 nm have been successfully fabricated by decreasing the distance between two laser paths below the Type-A double-track spacing. This work provides an effective and simple method to control the type of laser-induced glass modification in mid-infrared dielectric transparent media, simply by tailoring the glass composition and the DLW parameters. Hence, it opens up a new way to fabricate subwavelength integrated components in mid-infrared devices.

2. Glass Preparation and Basic Characterizations

From our previous work on the quaternary glass system $\text{Ga}_2\text{O}_3\text{--GeO}_2\text{--BaO--K}_2\text{O}$,^[45] it has been highlighted that the presence of alkali and alkali-earth ions allows for the generation of NBOs, while alkali ions help significantly to increase the cation mobility in the glass. As for silver-doped phosphate glasses,^[32,38,39] the amount of NBOs does also significantly influence the photosensitivity of BGG glasses. Thus, two glasses have been prepared from the quaternary system $\text{Ga}_2\text{O}_3\text{--GeO}_2\text{--BaO--K}_2\text{O}$ with a significant difference in terms of NBOs quantity while maintaining the ability of crack-free glass modifications during the irradiation process. These two glasses have been doped with their highest solubility concentration of silver ions, determined from an unpublished preliminary work where the glass synthesis of several silver concentrations has been performed: the first one with a large amount of gallium

Table 1. Physical chemical properties of GGBK and BGGK glasses.

Physical and chemical properties	GGBK sample	BGGK sample
Experimental composition [mol%]	32.9 mol% GaO _{3/2} 35.1 mol% GeO ₂ 14.8 mol% BaO 16.6 mol% KO _{1/2} 0.6 mol% AgO _{1/2}	15.4 mol% GaO _{3/2} 40.5 mol% GeO ₂ 37.5 mol% BaO 5.3 mol% KO _{1/2} 1.3 mol% AgO _{1/2}
Glass transition temperature (±3 °C)	642	624
Density	4.25	4.86
Concentration of silver ions (10 ²⁰ cm ⁻³)	1.6	3.2
Main Raman contribution position (cm ⁻¹) & assignment	510/T–O–T ^{a)}	800/[GeO ₃ O ⁻] ^{b)}
Optical window transparency ^{c)} [μm]	0.31–5.7	0.34–5.8

^{a)}T = Ge or Ga in tetrahedral coordination; ^{b)}germanium tetrahedral unit with one non-bridging oxygen; ^{c)}defined for an absorption coefficient value of 10 cm⁻¹.

and germanium, namely GGBK, and the second one with a large amount of barium and germanium, namely BGGK. GGBK glass is experimentally made of 32.9 mol% of GaO_{3/2}, 35.1 mol% of GeO₂, 14.8 mol% of BaO, 16.6 mol% of KO_{1/2}, and 0.6 mol% of AgO_{1/2}, while BGGK glass is made of 15.4 mol% of GaO_{3/2}, 40.5 mol% of GeO₂, 37.5 mol% of BaO, 5.3 mol% of KO_{1/2}, and 1.3 mol% of AgO_{1/2}. Glass precursors are first weighed and then introduced in a platinum crucible to be melted for 15 h at 1400 and 1350 °C for GGBK and BGGK, respectively. The long melting duration is rather important for the homogeneous dispersion of silver ions in the glass network. To freeze the mixture without disturbing its homogeneity, a quick quenching is conducted by immersing the crucible bottom in water at room temperature. Performed on ground glass chunks, X-Ray diffraction experiments have revealed no crystallization peaks, confirming full vitrification of both glasses (see Experimental Section). The detection limit specified by the manufacturer is about 1% by volume. However, the exact detection limit depends on the

density, Z number, and crystal structure of the studied compound. Hence, a degree of crystallization below 5% is considered as a safe value for the limit of detection. By determination of the experimental density evaluated at 4.86 and 4.25 g cm⁻³ for BGGK and GGBK, respectively (see Experimental Section), their concentration of silver ions per cubic centimeter has been calculated at 3.2 × 10²⁰ and 1.6 × 10²⁰ cm⁻³, respectively. A differential scanning calorimetry (DSC) measurement has been performed (see Experimental Section), which allows for determining the glass transition temperature *T_g*. For GGBK glass composition, the *T_g* is measured at 642 °C, whereas for BGGK, *T_g* is 624 °C. After thermal annealing at 30 °C below the glass transition temperature for 4 h, glass chunks from both compositions are cut and polished on two parallel faces so as to obtain optical grade 1 mm thick samples. Table 1 summarizes the physical and chemical properties of the two glasses presented in this work.

3. Results

3.1. Pristine Glass Properties

To characterize the glass structure and the optical transmission window of both pristine gallo-germanate glasses, the polished glass samples have been subjected to Raman and absorption spectroscopies. In Figure 1a are depicted the normalized Raman spectra of both GGBK and BGGK glasses under a 532 nm laser excitation. Both glasses can be separated in three regions of low (200–400 cm⁻¹), intermediate (400–650 cm⁻¹), and high (650–1000 cm⁻¹) frequencies. The lowest spectral domain can be assigned to either out-of-plane oxygen motions in bent T–O–T bridge (T = Ge or Ga in tetrahedral coordination)^[46] or network-modifying cations vibrating in large interstitial sites.^[47] The intermediate spectral range can be assigned to several vibrational contributions of T–O–T bending with in-the-plane T–O–T oxygen motions.^[46,47] Finally, the highest spectral domain can be attributed to symmetric and antisymmetric

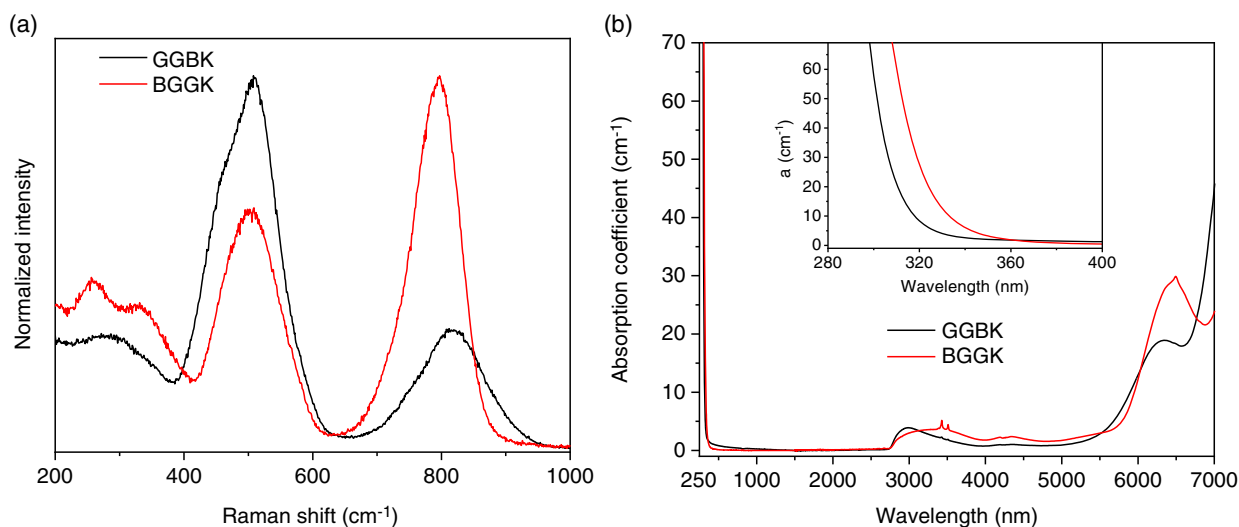


Figure 1. a) Raw data Raman spectra normalized at their maximum intensity and b) linear absorption coefficient in the UV-visible-to-mid-IR wavelength range for both GGBK and BGGK. Inset: Magnification of the UV–blue wavelength domain.

stretching modes of gallium and germanium tetrahedral units [TO₄].^[46,48] In this high-frequency region, the well-known contribution at the vicinity of 800 cm⁻¹ is assigned to the germanium tetrahedral unit with an NBO denoted [GeO₃O⁻].^[46,49] In GGBK glass, the Raman spectrum reveals an important Raman signal resulting from the intermediate-frequency region peaking at 510 cm⁻¹ with a significant shoulder at about 450 cm⁻¹, whereas in BGGK glass, the most important signal results from the high-frequency domain peaking at 800 cm⁻¹ followed by a tail around 700 cm⁻¹ and the vanishing of the Raman contribution at 900 cm⁻¹.

The linear absorption coefficient between 250 and 7000 nm has been assessed for both GGBK and BGGK. As presented in Figure 1b, the transmission window is extending from 310 nm (UV) to 5.7 μm (mid-IR) for GGBK, and from 335 nm to 5.8 μm for the BGGK, corresponding to linear absorption coefficients below the limit of 10 cm⁻¹. Since gallo-germanate glasses with close compositions but without silver normally present a UV cutoff near 270 nm,^[42,50] the upshifted UV absorption edges of our silver-doped glasses are attributed to presence of the silver ions. This assignment is also supported by the location in the same wavelength range as the silver ion absorption in phosphate

glasses,^[38,51] and also by the UV absorption edge undergoing a redshift from the GGBK to BGGK while the silver concentration increases, that is, with 1.6 × 10²⁰ and 3.2 × 10²⁰ cm⁻³ for GGBK and BGGK, respectively. Conjointly, the IR absorption edge is attributed to the multiphonon vibration modes. Between both gallo-germanate glasses, the IR absorption edge is affected by the glass composition revealing a 100 nm bathochromic shift from GGBK to BGGK and an increase of the 6.3 μm contribution band, as well. As no special care was taken during glass synthesis, OH impurities are detected around 3.2 μm.

Both steady-state and lifetime luminescence spectroscopic measurements have been performed to assess the silver luminescence, and thus, determine the silver species and their environment. In both glasses, several wavelengths of emissions and excitations have been investigated, but only two fixed wavelengths both in emissions (λ_{emi} = 350 and 450 nm) and in excitations (λ_{exc} = 270 and 320 nm) have been selected where the spectral differences appear to be the most significant corresponding to at least two major silver entities.^[45] The corresponding results are presented in Figure 2a,b for GGBK and BGGK glasses, respectively. In both glasses, the fluorescence spectrum under excitation at 270 nm reveals large bands with intensities

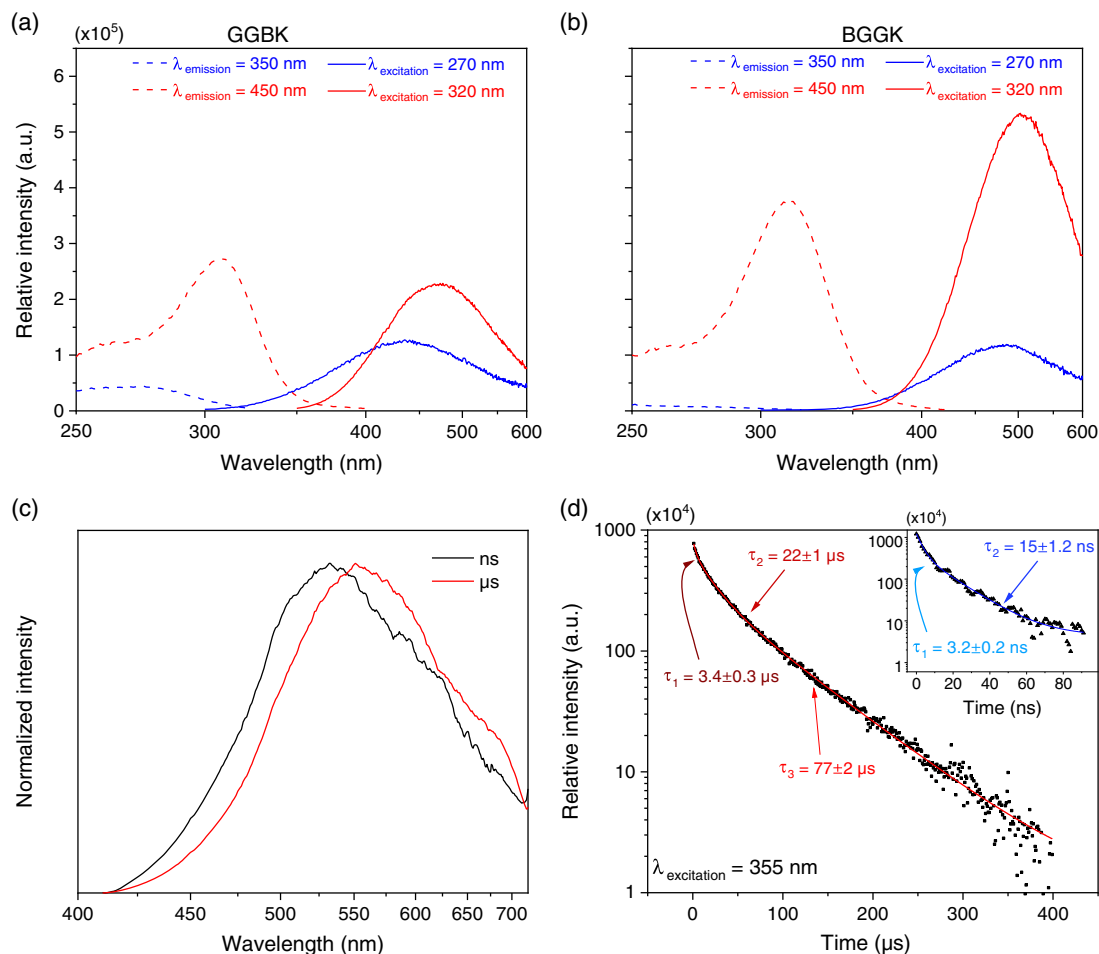


Figure 2. Excitation and emission spectra obtained at 350 and 450 nm, and at 270 and 320 nm, respectively, for a) GGBK and b) BGGK. Time-resolved spectroscopy of the BGGK glass under a laser excitation of 355 nm: c) spectra extracted from the nanosecond and microsecond lifetimes; d) long and short (inset) lifetimes obtained from the global spectral integration.

and locations that are composition dependent. In the barium-poor glass, the maximal intensity is reached at 440 nm with the presence of a contribution at 350 nm, whereas in the barium-rich glass, the maximal intensity peaks at 490 nm without any contribution at 350 nm. In the meantime, the associated excitation spectrum at this emission luminescence ($\lambda_{\text{exc}} = 270$ nm) has been measured. The corresponding spectrum has been recorded for an emission wavelength of 350 nm and highlights an excitation band at 280 nm for GGBK, while in BGGK, the excitation band is barely visible. By photoexciting both glasses at 320 nm, it gives rise to the emission of broadband from 350 nm to beyond 600 nm. The maximal intensity is denoted peaking at 470 and 500 nm for GGBK and BGGK, respectively. Conjointly, the associated excitation spectrum with an emission wavelength at 450 nm has been conducted. In this excitation spectrum, a significant band is observed at 307 and 315 nm for barium-poor and barium-rich glasses, respectively, going with a shoulder at 270 nm in both glasses.

To study the lifetime spectroscopy of BGGK glass, time-resolved spectroscopy has been performed with a laser excitation at 355 nm. Figure 2c shows the emission spectra acquired from a long (microsecond scale—red curve) and short (nanosecond scale—black curve) decay time. In both spectra, a wide emission band is observed in the visible range. From the nanosecond timescale to the microsecond timescale, a bathochromic shift of the maximal intensity is noticed from 525 to 550 nm, while the spectral distribution remains mostly unchanged. After a full spectral integration from 425 to 700 nm, the temporal evolution of the integrated fluorescence intensity is monitored. As presented in Figure 2d, the nanosecond timescale reveals two decay times of 3.2 and 15 ns, while the microsecond timescale shows three decay times of 3.4, 22, and 77 μs . However, concerning the shortest decay time of 3.2 ns and a laser pulse with a temporal half width at half maximum (FWHM) of 3–5 ns, this decay time could not be experimentally resolved with the used time-resolved apparatus, highlighting a decay time inferior at 3.2 ns. For the GGBK glass composition (results not shown in Figure 2), nanosecond and microsecond timescales are also detected. Three long decay times of 0.9, 16, and 47 μs , and one short decay time of 5.6 ns are extracted. Moreover, a noteworthy difference in terms of luminescence amplitude is noted. In both glasses, the luminescence amplitude is strongly dominated by the microsecond decays rather than by the nanosecond ones.

The steady-state and time-resolved spectrofluorometries of silver doped-gallo-germanate glasses with close composition up to 15 mol% of barium, such as in the GGBK glass, have already been published elsewhere.^[45] In this latter paper, the reported luminescence has been assigned not only to silver entities in different composition sites, such as $[\text{GaO}_4]^-$ and $[\text{GeO}_3\text{O}^-]$, but also with different nuclearities, such as isolated and aggregated silver species. In BGGK, the spectral distribution is highly similar to that of GGBK glass, with the existence of nanosecond and microsecond decay times. Hence, the presence of isolated and aggregated silver entities is expected. Nevertheless, from GGBK to BGGK glass compositions, bathochromic shifts are observed in the excitation and emission contribution bands. These bathochromic shifts highlight a strong difference in terms of ratios of silver entity populations, compared to the ones observed in barium-poor glass compositions, as in GGBK.

3.2. Direct Infrared Femtosecond Laser Writing and Characterizations

A scanning speed versus irradiance photo-inscription matrix was obtained for both GGBK and BGGK glasses. Due to the difference of photosensitivity between GGBK and BGGK, the irradiance range has been voluntarily adapted with nine irradiances (6.4/7.8/9.0/10.4/11.7/12.8/13.7/14.3/14.7 TW cm^{-2}) for GGBK and six irradiances (6.3/6.8/7.3/7.9/8.4/8.9 TW cm^{-2}) for BGGK. For both glasses, the same seven translation speeds (50/100/200/350/550/800/1100 $\mu\text{m s}^{-1}$) were employed. Each scanning speed versus irradiance data corresponds to a square structure that has been photo-inscribed from continuous laser irradiation. As shown, a back-and-forth inscription procedure is resulting in a $50 \times 50 \mu\text{m}^2$ square pattern with a 5 μm interline spacing. This kind of square structure was already performed in previous works.^[38] Both glasses have been subjected to IR femtosecond direct laser writing and show the capacity to be inscribed (see Experimental Section). For each glass composition, three DLW regimes were found: no fluorescence under UV excitation, fluorescence without Type III modification, and fluorescence with Type III. In the GGBK glass composition, only the 7.8 TW cm^{-2} , 50 $\mu\text{m s}^{-1}$ DLW structure reveals a regime of fluorescence without matrix explosion, while in the BGGK glass, many DLW structures show such a regime. Moreover, in BGGK, two sub-schemes at this regime were identified: strong fluorescence with a double-track fluorescent line or weak fluorescence with a single-track fluorescent line. As a result, only undamaged structures producing fluorescence are considered for further investigations. Hence, the characterizations have been conducted on the 7.8 TW cm^{-2} , 50 $\mu\text{m s}^{-1}$ DLW structure for GGBK, whereas on the 8.4 TW cm^{-2} , 50 $\mu\text{m s}^{-1}$ with a double-track fluorescent line sub-scheme and 6.8 TW cm^{-2} , 50 $\mu\text{m s}^{-1}$ with a single-track fluorescent line sub-scheme DLW structures for BGGK. To characterize these DLW square structures, microfluorescence and microabsorption spectroscopies, as well as phase-contrast and fluorescence confocal imageries, have been carried out.

The DLW photosensitivity in BGGK is defined by a large range of DLW parameters, certainly facilitated by a better silver solubility than in GGBK glass composition. This DLW range has been imaged under confocal fluorescence microscopy, as presented in Figure 3a, expanding from 7.3 to 8.4 TW cm^{-2} and from 50 to 350 $\mu\text{m s}^{-1}$. To highlight the fluorescence intensity evolution, integration of the fluorescence intensity has been performed on each DLW square structure with ImageJ software, as presented in Figure 3b. On the intensity diagram of Figure 3b, the increase of the fluorescence intensity with respect to the diminution of the scanning speed is observed and is remarkably similar to what was reported for silver-doped sodo-gallo-phosphates glasses.^[38]

From the DLW regime classification given by Abou Khalil et al., there is no doubt that at high irradiance, the DLW modifications are of the Argentum Type. Indeed, the Type A regime is a regime where the DLW modifications are only silver supported. Considering both superimposed double-track fluorescent and refractive index change lines with an inter-track spacing of 2 μm , as compared to the 1.8 μm observed in phosphate glasses,^[35] this confirms DLW Type A regime. At low irradiance,

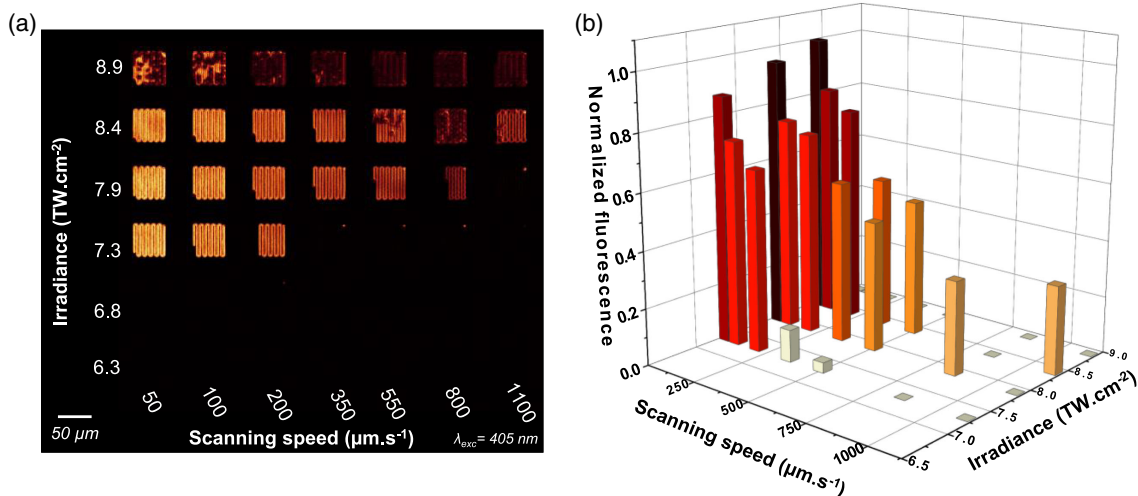


Figure 3. a) Confocal fluorescence imaging of the scan speed–irradiance matrix in BGGK glass with excitation at 365 nm; b) evolution of the integrated fluorescence imaging of all the photoinduced structures as a function of the translation speed and irradiance in the BGGK glass.

the description of the superimposed single-track fluorescent and Δn lines could superficially match with the Type I regime, but this regime is only glass matrix supported, which is not the case at low irradiance. Indeed, in the GGBK DLW structure, the inter-track spacing is wide at $2.2 \mu\text{m}$ and the single-track Δn is about 10^{-3} . Meanwhile, this same inter-track spacing at low irradiance in BGGK is only of $1.6 \mu\text{m}$ whereas the single-track Δn is about one order of magnitude less, that is, about 10^{-4} . Hence, one observes here the very early stages of Type A formation, with the preliminary mechanisms of silver cluster formation being initiated, as also reported in sodo-gallo-phosphate glasses.^[38]

Fluorescence confocal microscopy images of the selected DLW square structures in both GGBK and BGGK glasses under a laser diode excitation of 405 nm are presented in Figure 4a–c. As described earlier, the GGBK DLW structure exhibits lines of fluorescence on both sides of the laser beam path, as reported in the BGGK high-irradiance DLW structure as well. This double-track fluorescent pattern corresponds, in a 3D view, to a fluorescent double plane observed with a top view.^[35] In the meantime, the BGGK low-irradiance DLW structure exhibits a single line of fluorescence at the laser path location (cf. Figure 4c), which has been already demonstrated in silver-doped sodo-gallo-phosphate glass matrix at relatively low irradiance.^[38] From the profile analysis of the fluorescence intensity in these three DLW structures Figure 4g–i, the center-to-center distance between two laser paths is $5 \mu\text{m}$, which corresponds to the expected experimental inter-track spacing. The distance between two maxima of fluorescence intensity on the same laser path is measured to be $2.6 \mu\text{m}$ for GGBK DLW structure and $1.95 \mu\text{m}$ for BGGK high-irradiance DLW structure. Meanwhile, in the same laser focalization conditions, the inter-track spacing in phosphate glasses is $1.8 \mu\text{m}$.^[35] In the BGGK DLW structure photo-inscribed at low irradiance (Figure 4i), the FWHM of the fluorescent line is measured at $1 \mu\text{m}$.

The phase-contrast images are reported in Figure 4d–f for both GGBK and BGGK glasses. Phase-contrast imaging gives access to the optical path difference (OPD), which is directly

related to the refractive index change Δn from Equation (1), where l is the height of the photoinduced fluorescent single- or double-planar structure.

$$\Delta n = \text{OPD}/l \quad (1)$$

For both the GGBK DLW structure (Figure 4d) and BGGK low-irradiance DLW structure (Figure 4f), a single positive refractive index change line is noted, while for the BGGK high-irradiance DLW structure, a double-track positive refractive index change line is observed. To determine the height of the DLW fluorescent structures, the cross section of the DLW structures has been analyzed via fluorescence confocal microscopy and has been measured to be about $13 \mu\text{m}$ in both glasses. Thus, in accordance with Equation (1), the mean refractive index change Δn has been estimated to be 2.0×10^{-3} for the GGBK DLW structure, while 2.1×10^{-3} and 1.0×10^{-4} for BGGK structures obtained at high and low irradiance, respectively.

The refractive index change profile has also been plotted after careful baseline removal Figure 4g–i. For the GGBK DLW structure, the maximum refractive index change matches the laser beam center with a fluorescent line on both sides. The FWHM is determined to be $2.2 \mu\text{m}$. Furthermore, the maxima of refractive index change match the fluorescence intensity profiles in BGGK DLW structures. For the DLW structure photoinduced at low irradiance, the FWHM is measured to be $1.6 \mu\text{m}$.

Except for hole-trapped silver defect, namely Ag^{2+} , the other types of silver species like Ag^+ silver ions, clusters, and nanoparticles do not fade in glass over time at room temperature without any other stimulus.^[52] We have already reported the thermal stability of the laser-inscribed silver clusters in phosphate glasses as long as the temperature remains below the glass transition temperature.^[37] However, in the specific case of germanate glasses, the stability of silver species has not been studied yet. Nonetheless, during our measurements, no modification of the absorption or luminescence spectra has been observed. Hence, the stability of the latter silver species is also expected

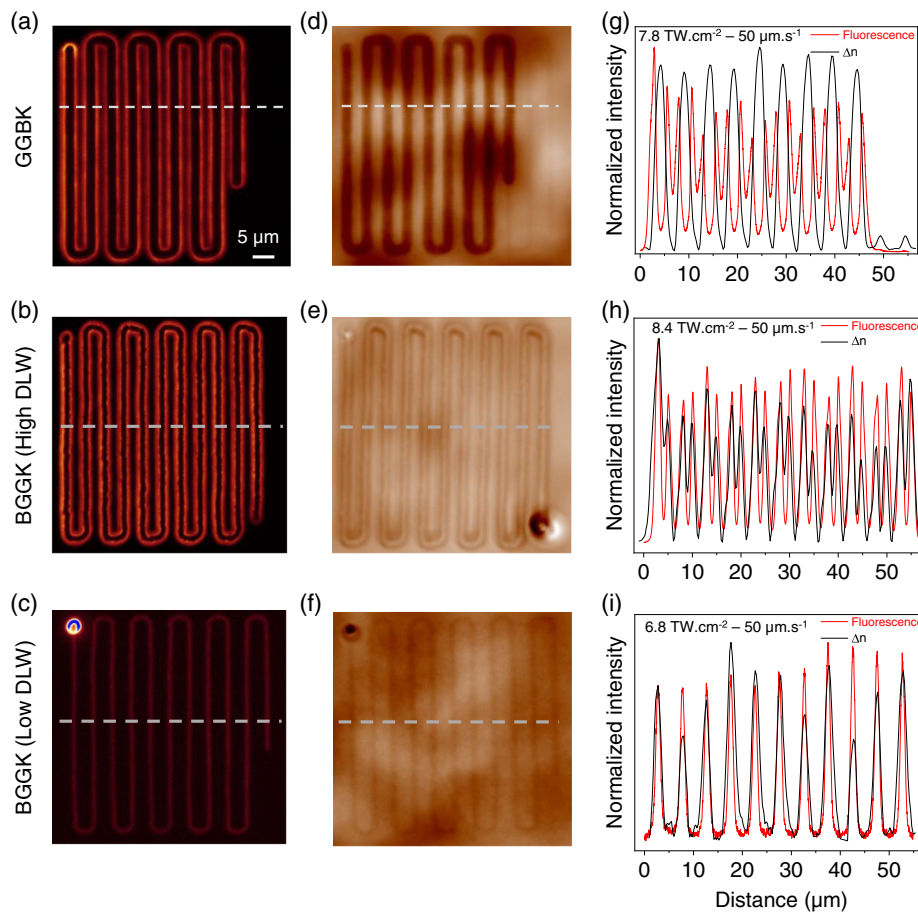


Figure 4. High-resolution imaging of both confocal fluorescence and phase contrast microscopies for photo-inscribed structures at a,d) 7.8 TW cm^{-2} , $50 \mu\text{m s}^{-1}$ in GGBK, and at b,e) 8.4 TW cm^{-2} , $50 \mu\text{m s}^{-1}$, and c,f) 6.8 TW cm^{-2} , $50 \mu\text{m s}^{-1}$ in BGGK; superposition of both fluorescence intensity and refractive index variation profiles for g) 7.8 TW cm^{-2} , $50 \mu\text{m s}^{-1}$ direct laser writing (DLW) structure in GGBK, and h) 8.4 TW cm^{-2} , $50 \mu\text{m s}^{-1}$ DLW structure and f) 6.8 TW cm^{-2} , $50 \mu\text{m s}^{-1}$ DLW structure in BGGK, extracted from images (a–f) at the location of the gray dashed lines.

to be long lasting or even permanent in BGGK and GGBK glasses as some fluorescent patterns inscribed months ago are still observable. To identify the long-term stable photoinduced silver species, microabsorption and microfluorescence spectroscopic measurements were conducted. As depicted in **Figure 5a**, the DLW structures in both GGBK and BGGK glasses present novel absorption contributions, which strongly overlap between 300 and 550 nm. For the barium-poor glass composition, a predominant contribution peaking at 435 nm is observed with a narrow profile and a shoulder centered at about 315 nm. Conjointly, the absorption spectra are different depending on the irradiance intensity in the barium-rich glass composition. For the DLW structure inscribed at high irradiance in BGGK, no contribution clearly arises, highlighting a wide hump with a maximum near 330 nm, whereas for the DLW structures inscribed at low irradiance, a clearly defined peak at 330 nm is observed with a long tail up to 475 nm. Despite the microabsorption spectrum differences, DLW structures emit in the visible range with a large emission spectrum peaking at 580 nm under a laser diode excitation of 405 nm (**Figure 5b**). For information, the maximal fluorescence intensity in BGGK is about 100 times more intense for the high-irradiance DLW structure than for the low-irradiance

DLW structure (as also visible with the very distinct signal-to-noise ratios for BGGK in **Figure 5b**).

3.3. Fabrication of Embedded Periodic Structure

The inter-track spacing in BGGK is about $1.95 \mu\text{m}$ at high irradiance of DLW. By decreasing the spacing between to laser paths (interline spacing) below the inter-track spacing, the silver clusters photodissociation and photodiffusion processes jointly contribute to decrease the actual spacing between the two remnant modification tracks. Hence, DLW of structures with a smaller spacing than the actual interline spacing of $5 \mu\text{m}$ have been performed in BGGK glass with an irradiance of 7.3 TW cm^{-2} and a translation speed of $100 \mu\text{m s}^{-1}$. Three structures have been inscribed with a pitch of $2 \mu\text{m}$, $1 \mu\text{m}$, and 400 nm . Their analyses by both fluorescence and phase-contrast imaging are highlighted in **Figure 6**.

To characterize the periodicity of the structures, the recorded phase-contrast and high-resolution fluorescence images have been analyzed. Note however that with a 300 nm resolution per pixel for the phase-contrast imaging, only the $2 \mu\text{m}$ pitch periodic structure can be resolved whereas the fluorescence imaging

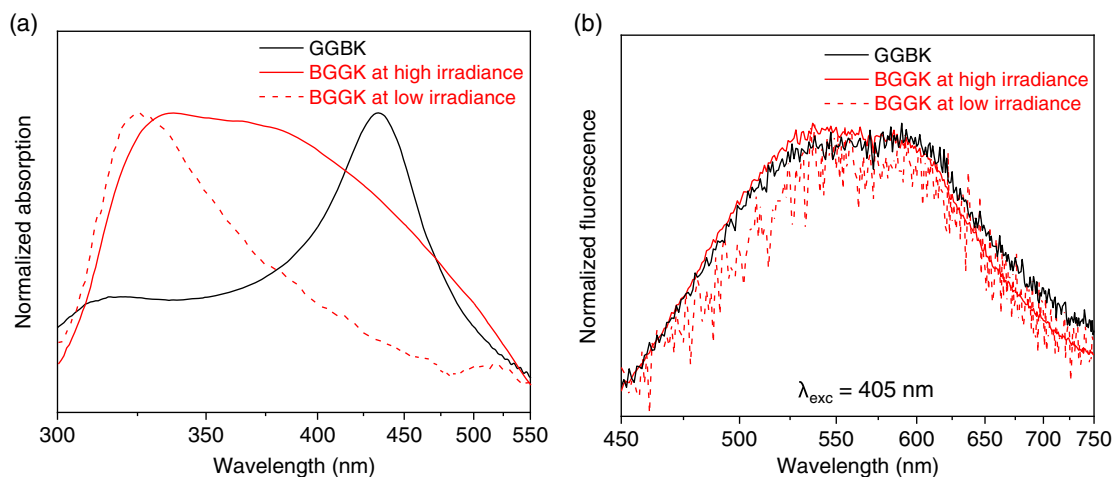


Figure 5. Normalized a) microabsorption and b) fluorescence spectra of DLW structures inscribed at 7.8 TW cm^{-2} , $50 \mu\text{m s}^{-1}$ for GGBK glass, and at 8.4 TW cm^{-2} , $50 \mu\text{m s}^{-1}$ and 6.8 TW cm^{-2} , $50 \mu\text{m s}^{-1}$ for BGGK glass.

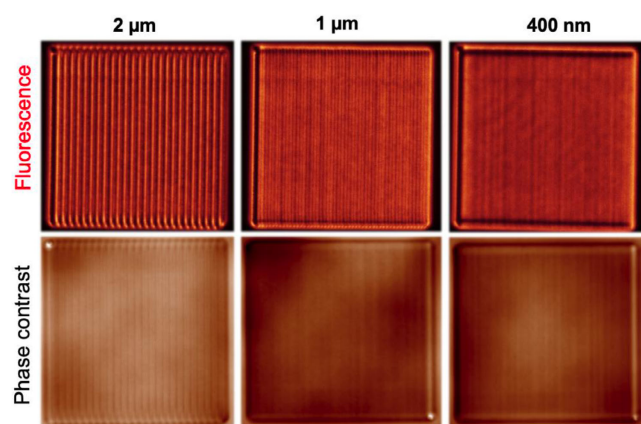


Figure 6. Structures photo-inscribed at 7.3 TW cm^{-2} and $100 \mu\text{m s}^{-1}$ with a pitch of $2 \mu\text{m}$, $1 \mu\text{m}$, and 400 nm in BGGK glass. High-resolution confocal fluorescence imaging on the top under laser excitation wavelength of 405 nm and phase-contrast microscopy at the bottom. Each square structure has a length of $50 \mu\text{m}$.

enables a theoretical lateral resolution up to 120 nm thanks to the 1.4 NA micro-objective (see Experimental Section). In **Figure 7** are presented the periodicity analyses for both $2 \mu\text{m}$ and 400 nm pitch periodic structures. To determine the experimental periodicity, a periodical test function has been simulated. For the $2 \mu\text{m}$ pitch structure, the refractive index change simulation gives a mean periodicity of $2.0 \mu\text{m}$, while for the 400 nm pitch structure, the fluorescence intensity variation simulation highlights a periodicity of 397 nm .

4. Discussion

4.1. Pristine Glass Properties

When the $(2\text{Ba}^{2+} + \text{K}^+)/\text{Ga}^{3+}$ ratio equals or is superior to 1, the gallo-germanate glass structure is composed of germanium and gallium tetrahedra, that is, $[\text{GeO}_4]^-$ as well as $[\text{GaO}_4]^-$, thanks to

enough positive-charge compensators (K^+ and/or Ba^{2+}) to the negatively charged gallium tetrahedra. Since the germanium tetrahedron is chemically neutral, it is not considered in the previous ratio. From the Raman spectroscopy study (Figure 1a), substantial structural differences have been highlighted between both GGBK and BGGK glass compositions. In GGBK glass, the Raman spectrum has evidenced a predominant Raman response from $[\text{GaO}_4]^-$ and $[\text{GeO}_4]^-$ tetrahedra, while the Raman signal originating from $[\text{GeO}_3\text{O}^-]$ entities is weak. In comparison with this later glass, the BGGK Raman spectrum shows a clear inversion of the Raman response intensity coming from both gallium or germanium tetrahedra without NBOs and the germanium tetrahedra with one single NBO. Considering that from GGBK to BGGK glasses, the $(2\text{Ba}^{2+} + \text{K}^+)/\text{Ga}^{3+}$ ratio rises from 1.3 to 5.1, clear network depolymerization of the gallo-germanate glass structure is occurring in BGGK glass, being induced by the formation of $[\text{GeO}_3\text{O}^-]$ tetrahedra with barium and potassium as charge compensators. Such kind of glass structure interpretation is highly supported by the previous work of McKeown and Merzbacher, where the BGGK counterpart of their study without potassium and silver has presented the relatively same Raman spectrum and interpretation.^[47] Moreover, considering our previous work on silver-doped GGBK glasses with the substitution of four different barium contents (i.e., 0, 5, 10, and 15 mol%)^[45] and as long as the $(2\text{Ba}^{2+} + \text{K}^+)/\text{Ga}^{3+}$ ratio is superior to 1, one can clearly attribute to the barium ion the role of network depolymerizing agent. Thus, regarding the drastic change of the cationic composition of both glasses, a gallo-germanate polymerized glass network and a bario-germanate depolymerized glass network are considered for the GGBK and BGGK glasses, respectively. Such kind of glass network difference could likely explain the observed modification of the IR absorption cutoff.

From GGBK to BGGK glasses, the glass transition temperature decreases by $18 \text{ }^\circ\text{C}$ along with an increase of the molar volume from 23.2 to $24.4 \text{ cm}^3 \text{ mol}^{-1}$. These physical-chemical property changes highlight a less reticulated and constrained glass network, which is consistent with the strong glass structure depolymerization reported in BGGK glass composition. While in GGBK glass, the silver ion introduction seems limited below

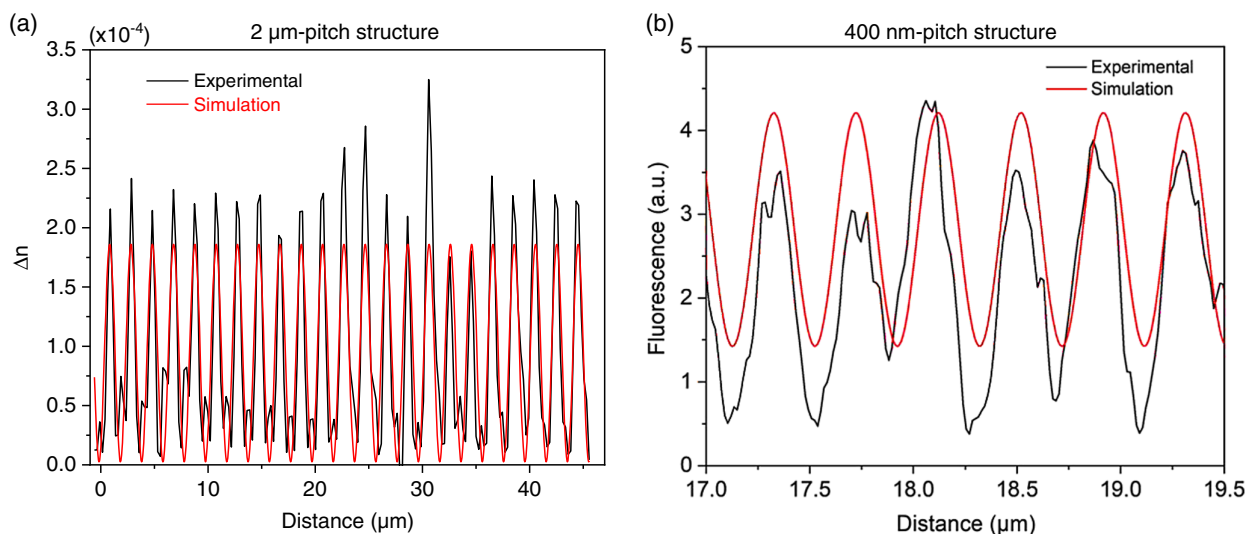


Figure 7. Periodicity analyses of the a) 2 μm pitch structure recorded by phase-contrast imaging and b) 400 nm pitch structure recorded with the high-resolution fluorescence imaging. Both structures have been photoinscribed at 7.3 TW cm^{-2} and $100 \mu\text{m s}^{-1}$ in the BGGK glass.

1 mol% using the classical melt-quenching glass synthesis, and in BGGK glass, the silver ion introduction can be greater than 1 mol%. Hence, it appears that the strong change in the glass network due to the increase of barium ions contributes to the solubilization and stabilization of silver ions in the glass matrix. One possible explanation would be that instead of compensating the negatively charged gallium tetrahedron, silver ions may create stable ionic bonds with NBOs mostly coming from the $[\text{GeO}_3\text{O}^-]$ entities which are in a great amount in BGGK glass.

The silver luminescence measurement reveals few spectral distributions and decay times change, evidencing highly similar silver entities in both GGBK and BGGK glasses. The presence of nanosecond decay time with a broad emission in the visible range is very characteristic of molecular silver entities like silver clusters as demonstrated in liquid solution^[53–55] and silver-doped phosphate glasses,^[56] while microsecond decay times are typical of isolated Ag^+ and/or paired Ag^+-Ag^+ silver species.^[45,57,58] However, comparing BGGK glass to its counterpart, the strong increase of the 330 nm excitation and 480 nm emission bands, as well as the vanishing of the 270 nm excitation contribution, strongly demonstrated that the silver entities, that is, isolated and aggregated, are not in the same proportion in both glasses. The major contribution in terms of amplitude of the microsecond decays against the nanosecond ones highlights a greater amount of isolated Ag^+ or paired Ag^+-Ag^+ rather than silver clusters. Hence, it is believed that silver ions are stabilized preferentially in another structural site for BGGK glass. Indeed, rather than being involved in the $[\text{GaO}_4]^-$ delocalized charge compensator site, silver ions are more likely engaged in the stable ionic bonding involving the NBO of the $[\text{GeO}_3\text{O}^-]$ germanium tetrahedra.

4.2. Direct Infrared Femtosecond Laser Writing and Characterizations

In silver-containing phosphate glasses supporting Type-A IR femtosecond DLW, the laser-induced novel fluorescence and

absorptions are due to the generation of silver clusters.^[12,38,56,59] With a similar broad emission band and absorption band localized in the same wavelength range as in phosphate glasses, it is likely that the photoinduced absorptions and fluorescence in both GGBK and BGGK glasses are also attributed to silver clusters. However, as previously described by Marquestaut et al.,^[37] the strong overlap of the novel absorption contributions makes difficult the band attributions and thus their assignment to precise silver entities. Hence, considering a strong similarity of photo-generated species between phosphate and gallo-germanate matrices, the 435 nm band clear contribution with a thin profile in GGBK is the only absorption band that can be assigned. It is attributed to a surface plasmon resonance (SPR) band, caused by reduced silver species, such as metallic nanoparticles of silver Ag_n , as reported elsewhere in phosphate glasses,^[37,60] and in a germanate glass as well.^[61] The SPR bandwidth must be compared with the volume concentration of nanoparticles and the filling factor with respect to the mean radius. From a Maxwell–Garnett simulation, as performed by Vangheluwe et al., and considering a monodisperse size distribution,^[61] the Ag_n mean radius is estimated at about 1.13 nm with a filling factor of 0.385×10^{-3} (Figure S1, Supporting Information). However, the presence of a high concentration of metallic silver nanoparticles, known to be nonluminescent, is surprising since a strong silver cluster fluorescence is denoted under a 405 nm excitation. Indeed, Marquestaut et al. had reported the cancelling of silver cluster fluorescence emission while these silvers clusters were grown into plasmonic metallic silver nanoparticles in a phosphate glass, thanks to a post-DLW thermal treatment.^[37] Hence, in the present case, it is proposed that the DLW species may be inhomogeneously localized in the GGBK sample. Considering the profile of luminescence intensity in this latter composition, the nonluminescent species would be in the center or the very close periphery of the laser beam path, while the concentration of silver clusters would be mostly at a certain distance away from the center of the laser path as directly observed by fluorescence imaging.

One last interesting point concerns the difference of microabsorption spectral distribution between both low- and high-irradiance DLW structures, while their microfluorescence spectra are strongly similar. Indeed, considering the excitation wavelength for the microfluorescence is at 405 nm (where the absorption is stronger in the high-irradiance DLW structures) and the silver clusters fluorescence is stronger when the DLW is at higher irradiance, it is suggested that at low DLW irradiance, the formation of nonluminescent silver entities, such as Ag^0 -reduced species, or/and colored silver centers, that is, Ag^{2+} may be favored. This hypothesis is highly supported by the appearance of the strong absorption band at 330 nm, being concomitant with the presence of both electron and hole silver defects, that is, Ag^0 and Ag^{2+} , as previously observed in sodo-gallo-phosphate glasses.^[39]

4.2.1. Hybrid Type A/I Modification

As reported by Abou Khalil et al. in silver-containing phosphate glasses subjected to IR femtosecond DLW,^[62] two types of DLW regimes can be observed, depending on the laser irradiation conditions. First, the Type A regime is associated with a refractive index change underlain by silver photochemistry, with a double line of fluorescence and refractive index. Second, the Type I regime is related to a smooth local modification of the glass density often driven by thermal effects, along with a single line of both fluorescence.

In the GGBK glass, the observed modifications present a single refractive index line with a double fluorescence line, positioned on either side of the inscription line. Recently, Bérubé et al. have reported the inscription of a single refractive index line in a nearly similar gallo-germanate glass matrix.^[29] In their work, in absence of silver, a Type I inscription regime has been evidenced by a local densification of the glass. In our study, Raman spectroscopy at 532 nm has been conducted on GGBK glass (Figure S2, Supporting Information) but modification of the glass density could not be detected. For silica glasses, the Raman spectrum changes (i.e., band positions and intensities) are progressive and appear strongly after a certain irradiance.^[63,64] Hence, it is supposed that in the BGGK glass, the deposited energy was not high enough to initiate strong glass structure modification, as monitored by Raman spectroscopy.

In light of Bérubé et al. study and our results, we propose the following explanations for the new regime observed in GGBK glass: 1) During laser irradiation, the energy transfer and electron thermalization phenomena followed by the silver photodissociation and diffusion processes are considered as the initiators of the laser modification. This leads to the first steps of the silver clusters creation. 2) The generation of new silver entities, that is, hole–electron trap silver centers and silver clusters, contributes significantly to the local temperature elevation (below the glass transition temperature) through the generation of new absorption bands in the visible spectral region leading to a more efficient absorption of the laser. Coupled with the thermally activated cationic migrations, it allows for material densification, especially in the laser path center, where temperature elevation is the highest, as for classic Type I modification.^[65] 3) Such a temperature elevation strongly favors nucleation/growth processes of silver nanoparticles in the center of the laser beam. 4) This temperature

elevation, however, decreases the amount of elementary component Ag^0 essential in the early stages of silver cluster formation. Once the Ag^0 species no longer exist, either by thermal destruction of these electron trap centers $\text{Ag}^0 \rightarrow \text{Ag}^+ + e^-$ or through the rapid formation of silver nanoparticles, the creation of silver clusters Ag_m^{x+} with high nuclearity is stopped. Such a kind of Ag^0 inhibition has been already highlighted by Petit et al. during an IR femtosecond DLW coupled with a UV co-illumination.^[66]

4.2.2. Type A Transposition in Mid-Infrared Glass

Unlike GGBK, the DLW of Type A in BGGK glass leads to the formation of a double track of both the refractive index change and the fluorescence where both properties are as expected spatially superimposed since they both originate from the formation of silver clusters. Until now, this remnant modification of the glass was only reported in silver-doped phosphate glasses. Developed in several types of phosphate glass compositions, such as zinc phosphate,^[12] sodium magnesium phosphate, sodium gallium phosphate,^[38] and the DLW in silver-containing phosphate matrices promote the Type A modification by means of the glass redox potential favorable to stabilize in a great quantity the silver ions. During the DLW process, the silver ions act as a fuse, like other transition metals,^[67] capable of restraining the laser modification on itself through photochemical reactions leading to the formation of stable photoinduced silver clusters.^[32] Consequently, when the concentration of fuse-acting chemical elements is not high enough, the laser pulse energy is only partially restrained on the doping element, and severe glass matrix modifications could be generated. In BGGK, the silver ion solubility is better than in GGBK by a factor of two, which could explain the difference of behavior in both glasses during the DLW. Moreover, the discrepancies in terms of silver species types and proportions stabilized in both pristine glasses could also have significant impact on their photosensitivity (Figure 2). Finally, compared to the silver concentration in phosphate glasses,^[38] the silver quantity in BGGK still remains lower and could justify the restricted range of laser parameters observed in Figure 3. Indeed, while in BGGK, this range is extending from 7.3 up to 8.4 TW cm⁻² and 50 up to 350 $\mu\text{m s}^{-1}$, it reaches 16.3 TW cm⁻² and 500 $\mu\text{m s}^{-1}$ for a silver-doped gallo-phosphate of sodium.^[38]

4.2.3. Embedment of Subwavelength Periodic Structures in Mid-Infrared Glass

The formation of the silver cluster-based double track of the Type A modification is originated from both the photodiffusion and photodissociation of the silver entities during the laser pulses accumulation.^[33] As reported by Desmoulin et al.,^[34] the competition of these two phenomena results in a partial depletion of the silver reservoir up to 20% at the remnant double-track center. During the formation of glass-embedded DLW structures with a spacing between to laser paths smaller than the inter-track one (Figure 6 and 7), the laser beam successively irradiates a partially silver-depleted glass region because of the previous laser pass. While no fading of both fluorescence intensity and refractive index change is noted over the entire DLW structure, it is believed that the entire silver reservoir is remobilized and still

contributes to the formation of perennial silver clusters after successive laser passes. To the best of our knowledge, this is the first time that remobilization of the silver reservoir is used to develop periodic structures. As discussed by de Castro et al.,^[68] the capability to remobilize the silver reservoir was believed to originate from the presence of highly co-mobile ions such as fluorine and alkaline ions in silver-doped oxyfluoride phosphate glasses. In our work, we have shown that the presence of barium ions, in majority in contrast to the potassium, promotes the remobilization of the silver reservoir. While the barium ion mobility in BGG glass is lower than that of potassium,^[45] it seems that either the high-quantity of low-mobility barium ions and/or the low-quantity of high-mobility potassium ions contributes beneficially to manage the silver reservoir in BGG glasses. Hence, these results extend the understanding of the silver reservoir remobilization in silver-doped glasses, which is promising for the future development of novel optical diffractive elements.

5. Conclusion

We successfully synthesized silver-doped gallo-germanate oxide glasses of barium and potassium via the classical melt-quenching method. Two BGG glasses were fabricated with an extended infrared optical transmission up to 5.7 μm , either with a low or high content of barium cations. By increasing the ratio of barium ions, the silver solubility inside the glass has been improved by a factor larger than 2. In the meantime, the barium concentration increase affects the glass network by depolymerizing the glass network and thus promoting new structural sites for the silver species. After the DLW process, at low Ba^{2+} content, the glass modification consisted of a hybrid combination of the Type I and Type A modifications. A bright luminescence from the silver clusters is reported between 450 and 750 nm, as well as followed by a refractive index change up to 2.0×10^{-3} . At a high concentration of Ba^{2+} , the DLW-induced refractive index modifications are entirely supported by the silver species, namely corresponding to the Argentum Type. At low laser fluence, a single track of fluorescence and refractive index change (up to 1×10^{-4}) is reported, corresponding to the very preliminary stages of Type A formation. At high laser fluence, the more usual double track of fluorescence and refractive index change (up to 2.1×10^{-3}) is demonstrated. For the first time, by taking advantage of the double-track DLW modification, embedded periodic structures with a pitch down to 400 nm have been successfully fabricated by narrowing artificially the Type A inter-track spacing. This work provides new insights through the fabrication of freeform photonic components buried inside mid-IR glasses.

6. Experimental Section

Glass Characterizations: Chemical analyses were conducted thanks to both inductively coupled plasma optical emission spectroscopy (ICP-OES) with an Agilent 5110 VDV apparatus, and electron-probed microanalysis (EPMA) using an electron microprobe (Wavelength-Dispersive Spectroscopy [WDS]) CAMECA SX 100. The density, ρ , was determined by Archimedes method using diethyl phthalate as an immersion liquid at room temperature. The measurement precision is estimated to be $\pm 0.01 \text{ g cm}^{-3}$. DSC measurements were made on a single 70 mg glass chunk in platinum crucible using a Netzsch DSC Pegasus 404 F3 from

500 and 1100 °C. Thanks to DSC measurements, the glass transition temperature defined as the intersection of the base line with the inflexion tangent of the glass transition domain was extracted.

Raman spectra were recorded at room temperature from 200 to 1000 cm^{-1} with a resolution of 2.5 cm^{-1} using a LABRAM 800-HR Raman spectrometer (Horiba Jobin Yvon) and a microscope objective 50 \times , NA 0.75. The excitation source is a single longitudinal mode laser at 532 nm. The UV-visible-near-IR transmission spectra from 200 to 2500 nm were recorded on a Cary 5000 (Varian) spectrometer by steps of 1 nm, while the near-IR-mid-IR transmission spectra were obtained from 2.5 to 7 μm using a Fourier-transform infrared spectrometer with an accumulation of 200 scans and a resolution of 4 cm^{-1} .

The steady-state excitation and emission spectra were recorded with a SPEX Fluorolog-2 spectrofluorometer (Horiba Jobin Yvon) on glass powder. Each spectrum was conducted with a step and resolution of 1 nm, and at room temperature. The excitation source was a 450 W xenon lamp having a continuous excitation from 200 to 800 nm. To detect and amplify the luminescence signal, a Hamamatsu R298 photomultiplier was employed. The decay time results were extracted from time-resolved spectroscopy. A Continuum Surelite SL II-10 laser was used as a pulsed 355 nm excitation source (10 Hz, 70 mJ, 4–6 ns) followed by a half-wave plate and a polarized beam splitter to control the laser fluence, ensuring that the measurement behaves only as an excitation regime in a lifetime-probing regime (and not in an irradiance regime that would lead to glass modifications). Emission spectra were recorded using a monochromator and a gated intensified charge-coupled device (ICCD) camera (Andor) being optically triggered by the pulsed UV laser.

Direct Infrared Femtosecond Laser Writing: Direct laser writings were performed on 1 mm thick glass samples using a ytterbium doped potassium-gadolinium tungstate crystal (KGW:Yb) femtosecond oscillator (up to 2.6 W, 10 MHz, 390 fs FWHM at 1030 nm) combined with an acousto-optic modulator to control the number and the energy of pulses, thus enabling several irradiances. Spherical aberrations were mostly corrected using a spatial light modulator (LCOS; X10468-03, Hamamatsu Photonics). A high-precision 3D translation stage XMS-50 (better than 50 nm resolution) was used to perform the sample positioning and displacements with various velocities from 50 to 1100 $\mu\text{m s}^{-1}$. An Olympus microscope objective (20 \times , NA 0.75) was used to produce the photoinduced structures, 160 μm below the sample surface.

Analysis of the Photoinduced Direct Laser Writing Structures: Microluminescence was conducted with a LABRAM 800-HR spectrophotometer (Horiba Jobin-Yvon) and an Olympus microscope objective (50 \times , NA 0.75) using an excitation laser diode at 405 nm (100 mW, TEM00, OBIS, COHERENT). Microluminescence spectra were recorded thanks to a thermoelectric cooled charge-coupled device (CCD) Camera (Synapse Model 354 308). The experimental spectra were corrected from the detection arm spectral response by a correction function determined using reference samples with broad spectral emission, while the pristine glass luminescence was subtracted from the recorded spectra. Microabsorption spectra were recorded using a "CRAIC Technologies" microspectrophotometer equipped with a Xenon lamp, a condenser, and a 10 \times microscope objective. Using this appliance, the obtained results consist directly of differential absorption spectra with a subtraction of the pristine glass absorption.

Confocal fluorescence imaging was performed using a Leica DM6 CFS TCS SP8 confocal microscope equipped with a 405 nm laser diode. Microscope objectives 10 \times , NA 0.3 DRY and 63 \times , NA 1.4 OIL were used. Confocal fluorescence imaging was also performed using a Leica SP2 confocal microscope using a 405 nm laser diode to determine DLW structure height of the glasses, using a 100 \times , NA 1.4 OIL microscope objective. The refractive index modifications of the DLW structures were recorded using a phase-contrast microscopy equipped with a commercial SID4Bio Phasics camera and a microscope objective (100 \times , NA 1.3 OIL).

Supporting Information

Supporting Information is available from the Wiley Online Library or from the author.

Acknowledgements

This work has received funding from the French Government, managed by the French National Research Agency (ANR-17-CE08-0042-01 and ANR-19-CE08-0021) and the Nouvelle Aquitaine Region (APPR2020-2019-8193110), and from the Canadian Government, managed by Sentinel North program of University Laval and the Canadian Research Chair program (CERC). This project has also received funding from the innovation program under the Marie-Sklodowska-Curie grant agreement N°823941 (FUNGLASS). The corresponding author, T.G., holds a Sentinel North Excellence Postdoctoral Fellowship and held an Excellence doctoral scholarship from the French Ministry of Higher Education and Research during the preparation of this work.

Conflict of Interest

The authors declare no conflict of interest.

Data Availability Statement

The data that support the findings of this study are available from the corresponding author upon reasonable request.

Keywords

direct laser writing, glass, grating, mid-infrared, periodic structure, silver cluster

Received: February 10, 2022

Revised: April 19, 2022

Published online:

- [1] K. M. Davis, K. Miura, N. Sugimoto, K. Hirao, *Opt. Lett.* **1996**, *21*, 1729.
- [2] R. R. Gattass, E. Mazur, *Nat. Photonics* **2008**, *2*, 219.
- [3] Y. Shimotsuma, P. G. Kazansky, J. Qiu, K. Hirao, *Phys. Rev. Lett.* **2003**, *91*, 247405.
- [4] M. Campbell, D. N. Sharp, M. T. Harrison, R. G. Denning, A. J. Turberfield, *Nature* **2000**, *404*, 53.
- [5] S. Gross, M. J. Withford, *Nanophotonics* **2015**, *4*, 332.
- [6] A. Crespi, R. Osellame, F. Bragheri, *Opt. Mater. X* **2019**, *4*, 100042.
- [7] M. Haque, K. K. C. Lee, S. Ho, L. A. Fernandes, P. R. Herman, *Lab Chip* **2014**, *14*, 3817.
- [8] J. Lapointe, M. Gagné, M.-J. Li, R. Kashyap, *Opt. Express* **2014**, *22*, 15473.
- [9] M. Ams, G. D. Marshall, P. Dekker, J. A. Piper, M. J. Withford, *Laser Photonics Rev.* **2009**, *3*, 535.
- [10] A. Arriola, S. Gross, M. Ams, T. Gretzinger, D. Le Coq, R. P. Wang, H. Ebendorff-Heidepriem, J. Sanghera, S. Bayya, L. B. Shaw, M. Ireland, P. Tuthill, M. J. Withford, *Opt. Mater. Express* **2017**, *7*, 698.
- [11] T. Meany, M. Gräfe, R. Heilmann, A. Perez-Leija, S. Gross, M. J. Steel, M. J. Withford, A. Szameit, *Laser Photonics Rev.* **2015**, *9*, 363.
- [12] A. Royon, K. Bourhis, M. Bellec, G. Papon, B. Bousquet, Y. Deshayes, T. Cardinal, L. Canioni, *Adv. Mater.* **2010**, *22*, 5282.
- [13] J. Zhang, M. Gecevicius, M. Beresna, P. G. Kazansky, *Phys. Rev. Lett.* **2014**, *112*, 033901.
- [14] J. Lapointe, J.-P. Bérubé, Y. Ledemi, A. Dupont, V. Fortin, Y. Messaddeq, R. Vallée, *Light Sci. Appl.* **2020**, *9*, 64.
- [15] K. Bourhis, A. Royon, G. Papon, M. Bellec, Y. Petit, L. Canioni, M. Dussauze, V. Rodriguez, L. Binet, D. Caurant, M. Treguer, J.-J. Videau, T. Cardinal, *Mater. Res. Bull.* **2013**, *48*, 1637.
- [16] G. Papon, Y. Petit, N. Marquestaut, A. Royon, M. Dussauze, V. Rodriguez, T. Cardinal, L. Canioni, *Opt. Mater. Express* **2013**, *3*, 1855.
- [17] S. Kanehira, K. Miura, K. Hirao, *Appl. Phys. Lett.* **2008**, *93*, 023112.
- [18] T. T. Fernandez, B. Sotillo, J. Del Hoyo, J.-A. Valles, R. Martinez Vazquez, P. Fernandez, J. Solis, *IEEE Photonics Technol. Lett.* **2015**, *27*, 1068.
- [19] D. M. Krol, *J. Non-Cryst. Solids* **2008**, *354*, 416.
- [20] M. Lancry, B. Pommellec, J. Canning, K. Cook, J.-C. Poulin, F. Brisset, *Laser Photonics Rev.* **2013**, *7*, 953.
- [21] F. Liang, R. Vallée, S. L. Chin, *Opt. Express* **2012**, *20*, 4389.
- [22] R. Stoian, *Appl. Phys. A* **2020**, *126*, 438.
- [23] A. Stone, M. Sakakura, Y. Shimotsuma, K. Miura, K. Hirao, V. Dierolf, H. Jain, *Mater. Des.* **2018**, *146*, 228.
- [24] J. Cao, B. Pommellec, L. Mazerolles, F. Brisset, A.-L. Helbert, S. Surble, X. He, M. Lancry, *J. Am. Ceram. Soc.* **2017**, *100*, 115.
- [25] X. Huang, Q. Guo, D. Yang, X. Xiao, X. Liu, Z. Xia, F. Fan, J. Qiu, G. Dong, *Nat. Photonics* **2019**, *14*, 82.
- [26] T. T. Fernandez, S. Gross, K. Privat, B. Johnston, M. Withford, *Adv. Funct. Mater.* **2021**, 2103103.
- [27] E. N. Glezer, E. Mazur, *Appl. Phys. Lett.* **1997**, *71*, 882.
- [28] L. B. Fletcher, J. J. Witcher, N. Troy, S. T. Reis, R. K. Brow, D. M. Krol, *Opt. Express* **2011**, *19*, 7929.
- [29] J.-P. Bérubé, A. Le Camus, S. H. Messaddeq, Y. Petit, Y. Messaddeq, L. Canioni, R. Vallée, *Opt. Mater. Express* **2017**, *7*, 3124.
- [30] S. Wong, M. Deubel, F. Pérez-Willard, S. John, G. A. Ozin, M. Wegener, G. von Freymann, *Adv. Mater.* **2006**, *18*, 265.
- [31] H. Yao, R. Zaiter, M. Cavillon, B. Sapaly, F. Calzavara, P. Delullier, T. Cardinal, Y. Dai, B. Pommellec, M. Lancry, *Ceram. Int.* **2021**, *47*, 34235.
- [32] Y. Petit, S. Danto, T. Guérineau, A. Abou Khalil, A. Le Camus, E. Fargin, G. Duchateau, J.-P. Bérubé, R. Vallée, Y. Messaddeq, T. Cardinal, L. Canioni, *Adv. Opt. Technol.* **2018**, *7*, 291.
- [33] M. Bellec, A. Royon, B. Bousquet, K. Bourhis, M. Treguer, T. Cardinal, M. Richardson, L. Canioni, *Opt. Express* **2009**, *17*, 10304.
- [34] J.-C. Desmoulin, Y. Petit, L. Canioni, M. Dussauze, M. Lahaye, H. M. Gonzalez, E. Brasselet, T. Cardinal, *J. Appl. Phys.* **2015**, *118*, 213104.
- [35] A. Abou Khalil, J.-P. Bérubé, S. Danto, J.-C. Desmoulin, T. Cardinal, Y. Petit, R. Vallée, L. Canioni, *Sci. Rep.* **2017**, *7*, 11124.
- [36] L. Canioni, M. Bellec, A. Royon, B. Bousquet, T. Cardinal, *Opt. Lett.* **2008**, *33*, 360.
- [37] N. Marquestaut, Y. Petit, A. Royon, P. Mounaix, T. Cardinal, L. Canioni, *Adv. Funct. Mater.* **2014**, *24*, 5824.
- [38] T. Guérineau, L. Loi, Y. Petit, S. Danto, A. Fargues, L. Canioni, T. Cardinal, *Opt. Mater. Express* **2018**, *8*, 3748.
- [39] T. Guérineau, F. Cova, Y. Petit, A. Abou Khalil, A. Fargues, M. Dussauze, S. Danto, A. Vedda, L. Canioni, T. Cardinal, *Int. J. Appl. Glass Sci.* **2020**, *11*, 15.
- [40] J. Harb, T. Guérineau, A. Morana, A. Meyer, G. Raffy, A. D. Guerzo, Y. Ouerdane, A. Boukenter, S. Girard, T. Cardinal, Y. Petit, L. Canioni, *Chemosensors* **2022**, *10*, 110.
- [41] A. Abou Khalil, P. Lalanne, J.-P. Bérubé, Y. Petit, R. Vallée, L. Canioni, *Opt. Express* **2019**, *27*, 31130.
- [42] S. S. Bayya, G. D. Chin, J. S. Sanghera, I. D. Aggarwal, *Opt. Express* **2006**, *14*, 11687.
- [43] F. Calzavara, M. Allix, M. Dussauze, V. Jubera, M. Nalin, T. Cardinal, E. Fargin, *J. Non-Cryst. Solids* **2021**, *571*, 121064.
- [44] A. Le Camus, Y. Petit, J.-P. Bérubé, M. Bellec, L. Canioni, R. Vallée, *Opt. Express* **2021**, *29*, 8531.
- [45] T. Guérineau, A. Fargues, Y. Petit, E. Fargin, T. Cardinal, *J. Non-Cryst. Solids* **2021**, *566*, 120889.

- [46] T. Skopak, S. Kroeker, K. Levin, M. Dussauze, R. Méreau, Y. Ledemi, T. Cardinal, E. Fargin, Y. Messaddeq, *J. Phys. Chem. C* **2019**, 123, 1370.
- [47] D. A. McKeown, C. I. Merzbacher, *J. Non-Cryst. Solids* **1995**, 183, 61.
- [48] T. Guérineau, C. Strutynski, T. Skopak, S. Morency, A. Hanafi, F. Calzavara, Y. Ledemi, S. Danto, T. Cardinal, Y. Messaddeq, E. Fargin, *Opt. Mater. Express* **2019**, 9, 2437.
- [49] T. Skopak, P. Hee, Y. Ledemi, M. Dussauze, S. Kroeker, T. Cardinal, E. Fargin, Y. Messaddeq, *J. Non-Cryst. Solids* **2017**, 455, 83.
- [50] T. Skopak, F. Calzavara, Y. Ledemi, F. Célarié, M. Allix, E. Véron, M. Dussauze, T. Cardinal, E. Fargin, Y. Messaddeq, *J. Non-Cryst. Solids* **2019**, 514, 98.
- [51] K. Bourhis, *Photostructuration par laser infrarouge femtoseconde de verres photosensibles de phosphates de zinc, d'argent et de gallium*, **2011**.
- [52] A. Royon, K. Bourhis, L. Béchou, T. Cardinal, L. Canioni, Y. Deshayes, *Microelectron. Reliab.* **2013**, 53, 1514.
- [53] B. G. Ershov, N. L. Sukhov, A. V. Kiseleva, G. V. Ionova, *Russ. Chem. Bull.* **1996**, 45, 545.
- [54] B. G. Ershov, G. V. Ionova, A. A. Kiseleva, *Russ. J. Phys. Chem.* **1995**, 689, 239.
- [55] M. Treguer, F. Rocco, G. Lelong, A. Le Nestour, T. Cardinal, A. Maali, B. Lounis, *Solid State Sci.* **2005**, 7, 812.
- [56] M. Bellec, A. Royon, K. Bourhis, J. Choi, B. Bousquet, M. Treguer, T. Cardinal, J.-J. Videau, M. Richardson, L. Canioni, *J. Phys. Chem. C* **2010**, 114, 15584.
- [57] I. Belharouak, C. Parent, B. Tanguy, G. Le Flem, M. Couzi, *J. Non-Cryst. Solids* **1999**, 244, 238.
- [58] I. Belharouak, C. Parent, P. Gravereau, J. P. Chaminade, G. Le Flem, B. Moine, *J. Solid State Chem.* **2000**, 149, 284.
- [59] K. Bourhis, A. Royon, M. Bellec, J. Choi, A. Fargues, M. Treguer, J.-J. Videau, D. Talaga, M. Richardson, T. Cardinal, L. Canioni, *J. Non-Cryst. Solids* **2010**, 356, 2658.
- [60] G. Y. Shakhgildyan, A. S. Lipatiev, M. P. Vetchinnikov, V. V. Popova, S. V. Lotarev, N. V. Golubev, E. S. Ignat'eva, M. M. Presniakov, V. N. Sigaev, *J. Non-Cryst. Solids* **2018**, 481, 634.
- [61] M. Vangheluwe, Y. Petit, N. Marquestaut, A. Corcoran, E. Fargin, R. Vallée, T. Cardinal, L. Canioni, *Opt. Mater. Express* **2016**, 6, 743.
- [62] A. Abou Khalil, J.-P. Bérubé, S. Danto, T. Cardinal, Y. Petit, L. Canioni, R. Vallée, *Opt. Mater. Express* **2019**, 9, 2640.
- [63] T. Seuthe, M. Grehn, A. Mermillod-Blondin, H. J. Eichler, J. Bonse, M. Eberstein, *Opt. Mater. Express* **2013**, 3, 755.
- [64] N. Varkentina, M. Dussauze, A. Royon, M. Ramme, Y. Petit, L. Canioni, *Opt. Mater. Express* **2016**, 6, 79.
- [65] T. T. Fernandez, M. Sakakura, S. M. Eaton, B. Sotillo, J. Siegel, J. Solis, Y. Shimotsuma, K. Miura, *Prog. Mater. Sci.* **2018**, 94, 68.
- [66] Y. Petit, K. Mishchik, N. Varkentina, N. Marquestaut, A. Royon, I. Manek-Hönninger, T. Cardinal, L. Canioni, *Opt. Lett.* **2015**, 40, 4134.
- [67] B. Boizot, N. Ollier, F. Olivier, G. Petite, D. Ghaleb, E. Malchukova, *Nucl. Instrum. Methods Phys. Res., Sect. B* **2005**, 240, 146.
- [68] T. de Castro, H. Fares, A. A. Khalil, R. Laberdesque, Y. Petit, C. Strutynski, S. Danto, V. Jubera, S. J. L. Ribeiro, M. Nalin, T. Cardinal, L. Canioni, *J. Non-Cryst. Solids* **2019**, 517, 51.